Comparison of sub-grain scale digital image correlation calculated using commercial and open-source software packages

DOI:
10.1016/j.matchar.2020.110271

Document Version
Accepted author manuscript

Comparison of sub-grain scale Digital Image Correlation calculated using Commercial and Open-Source software packages

D. Lunt[a*], R. Thomas[a], M. Roy[b], J. Duff[a], M. Atkinson[a], P. Frankel[a], M. Preuss[a], J. Quinta da Fonseca[a]

[*]David.lunt@manchester.ac.uk

[a] School of Materials, University of Manchester, Oxford Road, Manchester, UK, M13 9PL

[b] School of Mechanical, Aerospace and Civil Engineering, University of Manchester, Oxford Road, Manchester, UK, M13 9PL

Highlights

- Detailed comparison of the strain maps produced using popular commercial software packages from Correlated Solutions and LaVision and the open-source software nCorr
- Quantification of local strain for two HRDIC datasets exhibiting different slip localisation with different sub-micron behaviour in terms of frequency distributions and grain profiling
- The consequence of differences in displacement values between software packages highlighted by calculating the Relative Displacement Ratio within single grains to subsequently determine the active slip system

Keywords

Plasticity, Slip, Electron Backscatter Diffraction (EBSD), High Resolution Digital Image Correlation (HRDIC), Slip Systems, HCP

Abstract

High-resolution strain mapping is an increasingly prominent technique for characterising the deformation behaviour of metals. In this study, HRDIC analysis was performed on materials exhibiting either more or less intense planar slip, using different software packages to highlight any issues that might arise depending on the algorithm that is used to calculate the displacements. The differences between the algorithms were investigated using frequency distributions, strain profiling and Burgers vector direction analysis to determine their significance in terms of any subsequent interpretation of the data. A dilute zirconium alloy showed maximum strain concentrations of less than 4.5 and similar to previous comparison studies of different software packages on optical images, little difference was observed in the resulting strain maps. However, in a more highly alloyed two-phase titanium alloy with significant planar slip and strain values of up to 20 times the applied strain, one of the algorithms had difficulty tracking the features particularly at low strains when the difference between the strain in a slip trace is markedly higher than that in the neighbouring region. The consequences of inaccurate displacement data around a slip trace region were highlighted by an incorrect prediction of the Burgers vector when using the relative displacement ratio for slip system identification.

Introduction

The performance of a material can be better understood by relating the local deformation behaviour to the underlying microstructure. A prominently used technique for determining the deformation behaviour is Digital Image Correlation (DIC) where the full-field surface displacements are measured

and then used to produce strain maps at different spatial resolutions ranging from millimetres to nanometres [1]–[3]. The general principle behind DIC is the tracking of distinct features from a deformed image to an original reference image. The image sets are divided into smaller sub-regions allowing the relative displacement of the features within a single sub region in the deformed state to be cross correlated in relation to the reference image of the same sub-region. Once the full-field displacement map for the entire image has been generated, these values are differentiated to give the desired strain components. DIC does not have an intrinsic length scale [4], as the spatial resolution is dependent on both the pattern applied to the surface and also the analysis parameters used to calculate the displacements, thus providing the opportunity to study a materials behaviour over many grains and at a sub-grain scale. Macroscale DIC is generally performed using an objective lens and is most useful when the material properties are anisotropic with spatial resolutions 10μm and above, but it does not normally provide detailed sub-grain strain information [5]–[7]. However, there have been studies that have investigated this problem using optical [8]–[10] and confocal [11], [12] DIC and gained useful information at the sub-grain level, such as strain concentrations within grains and transgranular strain localisation due to planar slip, without the requirement of electron microscopy. Liu et al. also demonstrated the use of laser scanning confocal microscopy to identify the active slip system [12], where strain localisation higher than 10 times the macroscopic deformation was also observed, considerably higher than most optically based methods.

Combining imaging using a scanning electron microscope (SEM) with nanoscale speckle patterns and performing subsequent DIC analysis [13]–[22] often referred to as either HRDIC/HR-DIC (High Resolution Digital Image Correlation) or SEM-DIC, can enable single slip traces to be resolved and then quantitatively analysed to assess the level of strain heterogeneity. The high spatial resolution of the displacements and the fact that single slip traces can be captured provides the possibility of determining the direction of the Burger's vector, using the RDR (Relative Displacement Ratio) method proposed by Chen and Daly [21]. The RDR is equal to the ratio between the x component and y component of the slip plane direction for the respective slip system [21]. In combination with the angle of the slip trace from the initial strain map, this approach can be used to suggest the most likely slip mode for an individual grain by utilising the grain orientation information. This highlights the importance of having accurate displacement values, as these experimental predictions of active slip systems are often used to validate crystal plasticity finite element models (CP-FEM) and incorrect experimental results will lead to a false understanding of the deformation mechanisms. Other techniques that can be used to identify the slip activity include the Heaviside-DIC method [23], which has been developed to account for discontinuities in the displacement field and further adapted to enable the identification of the active slip mode and direction, and determination of the normalised displacement vector by using laser scanning confocal microscopy (LSCM) combined with DIC [12], which utilises the in-plane and out-of-plane measurements.

There are various commercial and open-source software packages available that can be used to evaluate the displacements and subsequently determine the strain values. The list of commercial software providers includes Correlated Solutions, CorreliSTC, Dantec Dynamics, GOM, Image Systems, Imetrum, LaVision and MatchID. The most widely recognised open-source packages available are Digital Image Correlation Engine (DICe), Ncorr, py2DIC, OpenDIC and YADICS. Although commercial software is typically faster and in principle should have more rigorous validation protocol, it is not free and the details of the algorithms used for the calculation are typically hidden from the user. Furthermore, commercial software packages are often general purpose and difficult to tailor to suit a particular user's requirements. In contrast, open-source software can be specifically adapted to link with other software packages and often has development forums to help advance the software and meet the changing needs of the community. However, it should be noted

that the commercial software provider EikoSim are also evolving in this field by enabling the processing of all test and simulation data within a single integrated package.

The most commonly used software packages for evaluating images captured for the purpose of HRDIC are VIC-2D (Correlated Solutions) [17], [22], [24] and DaVis (LaVision) [13], [14], [16] with a recent high-resolution study also analysed using Ncorr [25]. It can be difficult to make direct comparisons of results from separate studies, as the analysis parameters are referred to differently by each software package and although the quoted spatial resolutions are the same the final strain maps may look markedly different. Previous studies have compared the strain maps produced from optical imaging using different software packages [26]–[28], specifically one between py2DIC and VIC-2D [26] and another comparing Ncorr and VIC-2D [27]. A good agreement was found in terms of both the displacements and the resultant strain maps, where the only difference appeared to be due to slight discrepancies in the spatial resolution. This is expected, as in these DIC measurements[26]–[28] maximum strain concentrations of only 2-3.5 times the average strain were observed. Comparison studies have also been performed using SEM-DIC data [18], [23], where in particular Stinville et al. investigated the sub-grain scale deformation in a nickel-based superalloy using both VIC-2D and OpenDIC [18]. Although the results from the different software packages had many similarities, it was difficult to make a direct comparison due to the application of an automatic minimum filter of 5 pixels using VIC-2D (5 pixels) coarsening the raw data.

In the case of HRDIC, where individual slip bands can be captured, the strain concentrations can be greater than 10 times the applied strain [29], which is more likely to lead to discontinuities in the pattern that cannot be tracked in the image correlation analysis. The aim of this paper is to evaluate whether the increased spatial resolution leads to any marked differences in the displacement data between three different software packages. Strain profiles and frequency distributions will be used in combination with RDR analysis to quantify the differences between the software packages.

Experimental Procedure

Material

The materials investigated in this study were conventional two-phase (α+β) titanium alloy, namely Ti-6Al-4V, subjected to an aging treatment to promote the formation of very fine α_2 precipitation, and recrystallised Zircaloy-4, nominally Zr-1.5Sn-0.2Fe-0.1Cr (wt%), both supplied by Rolls-Royce Plc. Further details on the heat treatments, microstructures and the relative strain localisation behaviour of the two materials are given in [30], [31]. As a brief summary of the strain heterogeneity, the Ti-6Al-4V sample studied here displayed highly planar slip with typically higher strain values for prismatic slip compared to a sample without α_2 [30] and the Zircaloy-4 sample exhibited far more diffuse and homogeneous slip patterns [31] compared to Ti-6Al-4V.

Samples were hand polished with 0.06 µm colloidal silica solution (diluted with 20% hydrogen peroxide) for 30 minutes for EBSD analysis and subsequent application of the gold speckle pattern. Grain orientation mapping was performed in the HRDIC region for the Ti-6Al-4V sample using a field emission gun (FEI Quanta 650) SEM equipped with an AZtec EBSD system and a Nordlys II detector. EBSD scans were performed at an operating voltage of 20 kV, at a step size of 0.5 µm. The data (confidence index > 0.1) were analysed and plotted using HKL Channel 5^{TM} software.

Digital Image Correlation and Mechanical Loading

For 2D strain analysis using HRDIC, a speckle pattern was applied using the water vapour gold remodelling technique [32] for the Ti-6Al-4V sample and the styrene assisted gold remodelling

technique [33] for the Zircaloy-4 sample. Further details on the remodelling process are given in [32], [33]. The Ti-6Al-4V sample was then imaged, using a FEI Quanta 650 Field Emission Gun (FEG)-SEM at 20 kV at a working distance of 6 µm. The Zircaloy-4 sample was imaged using a FEI Magellan FEG-SEM, at an accelerating voltage of 5 kV in immersion mode with a 2 kV stage bias at a working distance of 3.4 mm, using a concentric back scattered (CBS) detector. All images were acquired in Backscattered Electron (BSE) imaging mode. The microscope required was dependent on the size of the gold speckles on the surface of the samples, which are typically finer after styrene remodelling. Images were taken at field widths of 29.8 µm (Ti-6Al-4V) and 10 µm (Zircaloy-4), respectively, with a resolution of 2048 × 1768 pixels^2 and a dwell time of 10 µs. Subsequently, the specimens were deformed (ex-situ) in tension to a specified applied strain (room temperature) at a strain rate of 0.1 mm/min using a Kammrath-Weiss 5 kN Tension-Compression microtester. The strains quoted here are for the unloaded conditions and were calculated by using the displacements, measured using a Linear Variable Differential Transformer (LVDT), and considering the initial gauge length. After each deformation stage, the sample was removed from the microtester and mounted in the SEM where images of the initial area were acquired at the same imaging conditions as the original state. For each sample, the image sets for each loading step were stitched together using the 'Grid/Collection stitching' function with a linear blend applied between images in ImageJ version 1.52p [34] and were subsequently aligned in terms of position and rotation by manual manipulation prior to processing using the different image correlation software. In order to ensure a fair comparison of the results from the different correlation algorithms identical image sets were utilised.

The HRDIC analysis was performed using Correlated solutions VIC-2D 6.0.6, LaVision's DaVis 8.4.0 [35] and the open-source MATLAB code Ncorr 1.2.2 [27]. The local displacements were determined by comparing the deformed state to the initial state. Two approaches used for determining the displacements are cross-correlation and the Least Square Matching (LSM) method. Cross-correlation tracks the point of interest by shifting pixel by pixel from the initial interrogation window within a specific range in the deformed interrogation window. The nearest location at the pixel level is determined based on the position of the best-matched pattern. This position is the maximum value of a cross-correlation coefficient. LaVision have developed a fast Fourier transformation (FFT) version of the cross-correlation method to calculate the local displacement. LaVision also provides the possibility of using the LSM approach, which is adopted by Correlated Solutions and Ncorr. The LSM method is based on the minimization of the squared differences of greyscale values between the deformed and initial state pixels. It typically provides matches with sub-pixel accuracy and is able to account for both translational and rotational transformations. From herein, the four different algorithms being compared are abbreviated to DaVis FFT, DaVis LSM, Ncorr and VIC-2D. Computation of the displacement maps was performed on a Dell T5610 with dual Intel Xeon E5 2670 v2 2.5 GHz CPUs, 128GB of DDR3 memory and a NVIDIA Quadro K4000 GPU running Windows 7 Professional 64-bit SP1 from a Samsung 850 PRO SSD.

As the images recorded for the two-different materials were taken at different magnifications due to the size of the speckles, different sub-pixel interrogation window sizes were also required to optimise the balance between maximising spatial resolution and minimising the error associated with the interpreted displacements. Additionally, the definition of interrogation window size varies between the different algorithms. Therefore, to maintain the same overall spatial resolution for the strain measurements, the interrogation window size and overlap were adjusted accordingly to give the same total number of interrogation windows. This is particularly useful in terms of being able to compare profile plots between the different algorithms, as the position of grain boundaries and deformation features like slip traces is identical. The parameters used are summarised in Table 1, where the size of an individual interrogation window is 174.6 x 174.6 nm^2 for Ti-6Al-4V and 78.1 x

78.1 nm^2 for Zircaloy-4. For the LSM approach, seeding points needed to be defined as these provide the initial guess in the deformed images. In this study, 16 seeding points were found to give the best initial guess and these were positioned in areas where independent features/speckles were easily identifiable for all deformation steps. The same positions were selected for each of the LSM approaches. The time taken to perform the DIC analysis is also noted in Table 1, which indicates that Ncorr is significantly slower than the other software packages.

The subsequent strain calculations and data analysis were performed using in-house Python routines and the NumPy numerical library [36]. The Matplotlib library [37] was used for visualisation. By differentiation of the in-plane displacements, the components of the strain tensor were determined. The differentiation was performed using the inbuilt NumPy function 'gradient', which is calculated using second order accurate central differences for the interior points and first order accurate one-sides (forward or backwards) differences at the boundaries. The datasets produced by the different algorithms were exactly the same size for each of the materials enabling a direct comparison in terms of both visualisation and also the strain values themselves. The correlation produces full-field in-plane displacement maps $u(x_1, x_2, 0)$ on the plane x_1x_2 with normal x_3. Therefore, the components of the displacement gradient describing the in-plane deformation can be calculated using Eq. 1.

$$\frac{\partial u_i}{\partial x_j} = \begin{bmatrix} \frac{\partial u_1}{\partial x_1} & \frac{\partial u_2}{\partial x_1} \\ \frac{\partial u_1}{\partial x_2} & \frac{\partial u_2}{\partial x_2} \end{bmatrix} (1)$$

The gradients were computed using second order accurate central differences to ensure that it was calculated at the same points for all components thus reducing the effects of displacement uncertainty on the calculation. In this study, the strain maps are typically presented in terms of the effective in-plane shear strain (γ_{eff}), calculated using Eq. 2, as this takes into account all the in-plane displacement gradient components as shown in [30], [32].

$$\boldsymbol{\gamma_{eff}} = \sqrt{\left(\frac{(\boldsymbol{\varepsilon_{xx}} - \boldsymbol{\varepsilon_{yy}})}{\mathbf{2}}\right)^2 + \left(\frac{(\boldsymbol{\varepsilon_{xy}} + \boldsymbol{\varepsilon_{yx}})}{\mathbf{2}}\right)^2} \quad (\mathbf{2})$$

Determining the active slip system

The high spatial resolution of HRDIC studies makes it possible to study individual slip traces within strain maps, which enables the slip plane and the potential Burgers vectors associated with the slip plane to be identified using a combination of the slip trace analysis technique and Relative Displacement Ratio (RDR) method. The slip trace analysis technique gives a quantifiable prediction of the active slip plane in an individual grain by using the orientation information gained from EBSD analysis and cross correlating it with the slip trace angle measured from the strain map [38]. However, due to overlapping theoretical slip angle predictions for particular crystal orientations this method does not always provide an unambiguous solution. A complimentary method for reducing this uncertainty is the calculation of the RDR [21], which utilises the displacement fields near the slip bands and is calculated theoretically as being equal to the ratio between the x component and y component of the slip plane direction for the respective slip system. It should be noted that this method provides the slip direction in comparison to the traditional slip trace analysis technique which gives only the slip plane.

Results and Discussion

Material and speckle pattern characterisation

Figure 1 shows the typical speckle pattern and representative orientation map from the HRDIC region for the two different material conditions. The ideal speckle pattern for DIC purposes has a randomly distributed pattern with a uniform speckle size and spacing. Comparing the speckle patterns for Ti-6Al-4V, Figure 1a, and Zircaloy-4, Figure 1b, indicates that the Zircaloy-4 sample has finer speckles, average diameter of 70 nm for Ti-6Al-4V and 30 nm for Zircaloy-4, and closer spacing due to using styrene rather than water vapour in the remodelling process. The interrogation window size is shown in the top left of each speckle pattern, 12 x 12 pixels^2 for Ti-6Al-4V and 16 x 16 pixels^2 for Zircaloy-4, where it can be observed that for both conditions the magnification has been adjusted to give a minimum speckle size of ~ 3 x 3 pixels^2 to ensure a good correlation [5]. The orientation maps indicate recrystallised, equiaxed microstructures for both materials with an average grain size of ~15 µm for Ti-6Al-4V, Figure 1c, and ~10 µm for Zircaloy-4, Figure 1d. The Ti-6Al-4V has an essentially random texture, whereas there is a 'split-basal' texture in the Zircaloy-4 sample, where the basal poles are preferentially oriented in ND with a spread of ± 28° in TD.

Strain Mapping

Previous studies on the strain localisation behaviour of the two alloys analysed here, indicate distinct differences in the degree of heterogeneity with relatively homogeneous slip in Zircaloy-4 loaded along the original rolling direction [31] compared to sharp, planar slip in Ti-6Al-4V [30].

Zircaloy-4

Figure 2 shows maps of effective in-plane shear strain for Zircaloy-4 at a nominal applied strain of ~2.5%, computed from the displacement data from the different software packages, and the corresponding normalised frequency distributions of the effective in-plane shear strain in comparison to Ti-6Al-4V, which was computed using the DaVis FFT algorithm. Comparing the maps of effective in-plane shear strain for the different algorithms indicates that there are no clear differences between them. Areas of high strain, single slip traces, low strain at $Zr(Fe,Cr)_2$ second phase particles and high strain at grain boundaries are easily identifiable for each algorithm in Figure 2a-c (DaVis FFT, Ncorr and VIC-2D, respectively). Whilst no obvious differences were observed from the strain maps, the difference in strain heterogeneity can be further compared in a more quantitative manner by plotting the frequency distributions of effective in-plane shear strain for the different algorithms. In this study, to enable a comparison of the heterogeneity between zirconium and titanium, the effective in-plane shear strain values have been normalised by dividing each value by the average effective in-plane shear strain across the complete HRDIC map. Also, as the highest strain values are likely to highlight any differences between the different algorithms, the frequency distributions have been plotted on a log-log scale. Figure 2d shows that even when analysing the data on pixel by pixel level, the 3 different algorithms still exhibit almost identical frequency distributions for Zircaloy-4. However, comparing the frequency distributions for Zircaloy-4 with a conventional titanium alloy (Ti-6Al-4V), analysed with similar DIC processing parameters and spatial resolution, indicates that the strain localisation is relatively homogeneous. Another measure of assessing the amount of strain heterogeneity is by calculating the ratio of the maximum to mean value of effective in-plane shear strain and which is ~4-5 for Zircaloy-4 compared to strain concentrations greater than 10 for Ti-6Al-4V.

Ti-6Al-4V

Figure 3 and Figure 4 shows maps of effective in-plane shear strain for Ti-6Al-4V computed from the displacement data for each algorithm at applied strains of ~1% and ~5%, respectively. Clearly, the

strain patterns here are very different to the ones observed for Zircaloy-4 in Figure 2. After ~1% tension, Figure 3a-c for DaVis FFT, DaVis LSM and Ncorr, respectively, all show similar effective in-plane shear strain maps with some grains exhibiting intense planar slip traces while other grains only show slip traces of low intensity or no deformation at all. In contrast, the effective in-plane shear strain map produced from the VIC-2D displacement data, Figure 3d, has many regions that have no/poor correlation, which are present in areas of both low and high strain when compared with the maps produced from the other algorithms. A no/poor correlation is considered to be a pixel be a pixel giving a 0.00 correlation value. The average correlation value observed for DaVis FFT was 0.91 and 0.89 at 1% and 5% with minimum values of 0.5 in regions of high deformation. Similarly, at ~5% applied strain the effective in-plane shear strain maps for DaVis FFT, DaVis LSM and Ncorr, Figure 4a-c, all show the development of new slip traces and significant shear strain intensification in existing slip traces, whereas the map for VIC-2D again has many regions where the correlation is poor. Several of the regions with no/poor correlation are the same as those observed at ~1%. However, there are now regions that appear to have a good correlation and others that have no/poor correlation. A no/poor correlation is defined as a point that gives a low correlation index value and therefore has large uncertainty in the displacement value.

Figure 5 compares frequency distributions of the normalised effective in-plane shear strain for the different algorithms for Ti-6Al-4V after ~1% (Figure 5a) and ~5% (Figure 5b) plastic deformation, respectively. This demonstrates that there are slight differences in the effective in-plane shear strain values between DaVis FFT, DaVis LSM and Ncorr that increases with increasing applied strain. In contrast, VIC-2D exhibits a non-uniform effective in-plane shear strain distribution with a large number of high shear strain values indicating significant correlation errors in this shear strain regime. The strain concentrations are around 20 times the macroscopic strain at the initial strain level, which reduces with increasing applied strain to around 10 times at ~5% applied strain [29]. Previous studies comparing DIC data from different algorithms have either been in relation to optical imaging [26]–[28] or SEM-DIC [18], where larger horizontal field widths and different patterns were used. Similar to the strain maps here for Zircaloy-4, these studies found little difference between the displacements and the resultant strain maps for each of the algorithms. This suggests that when the strain localisation is either relatively homogeneous and/or the measurements are resolved at a lower spatial resolution, there is an increased likelihood of a good correlation.

The features that contribute to the high strain spikes in the VIC-2D data are analysed further in Figure 6 where the BSE images for a specific area are compared to the effective in-plane shear strain maps at each deformation step. The overview BSE image of the speckle pattern, Figure 6a, indicates that the α-phase (black) and β-phase (white) regions are easily identifiable and subsequently the β-phase regions appear to correlate to the areas with no/poor correlation in the effective in-plane shear strain map at ~1%, Figure 6b. However, at ~5% applied strain, Figure 6c, the correlation is predominantly worse in the slip trace regions with significant spikes in the strain values in these regions where the traces do not appear planar compared to the other algorithms. The features contributing to the poor correlation were further investigated by comparing the BSE images at the pixel scale for the β-phase region highlighted by the white box in Figure 6a-c. The effective in-plane shear strain maps show a poor correlation at ~1% applied strain and an apparent slip trace at ~5% macroscopic strain. Red boxes equal to the size of an interrogation window are shown on the BSE images from before deformation and at 1% and 5% applied strain, Figure 6d-f. This shows that single speckles can be easily identified from one step to another and therefore should not lead to any issues in calculating the displacements. However, Figure 6e highlights that in the region of poor correlation the image is distinctly brighter compared to other regions, which may lead to difficulties when using VIC-2D in recognising the features due to the differences in relative intensities. However,

this did not cause any problems for the other 3 algorithms investigated. Even after thresholding, this image to the same brightness and contrast levels, where the speckles are the same shape and size, the resulting strain maps still exhibited a poor correlation using the VIC-2D algorithm.

Strain localisation in a single grain

Due to recent advances in patterning techniques that are consistent over large areas, it is now possible to perform high-resolution strain mapping across a statistically relevant number of grains with stage mapping in an SEM. It is also desirable to link the strain localisation to the underlying microstructure on a grain by grain basis. Correlating the EBSD orientation information with the HRDIC data enables single grains to be isolated and subsequent slip trace and RDR analysis to be performed. It also provides the opportunity for the strain mapping information to be directly compared with the orientation data and thus parameters such as Schmid factor and grain size can be correlated with the average and maximum effective in-plane shear strains for every grain. Figure 7 and Figure 8 shows representative maps of effective in-plane shear strain and the corresponding normalised frequency distributions for Ti-6Al-4V in a single grain at applied strains of ~1% and ~5%, respectively. Similar to the findings for the entire HRDIC region, the effective in-plane shear strain maps compare favourably for DaVis FFT, DaVis LSM and Ncorr at both 1% (Figure 7a) and 5% (Figure 8) applied strain. The development of new slip traces between pre-existing slip bands when increasing from 1% to 5% overall strain is also clearly observed. From the effective in-plane shear strain map for VIC-2D it is clear that not only are there single high intensity spikes in the slip trace regions, the algorithm also fails to capture one of the slip traces at the early strain step. At this strain step, the strain in between the slip traces is significantly higher than for the other algorithms. This is highlighted further from the normalised frequency distribution, Figure 7b, where the peak for VIC-2D is shifted to the right indicating a higher average shear strain. Although, the effective in-plane shear strain maps appear identical for the other algorithms, the normalised frequency distributions at both strain steps, Figure 7b and Figure 8b, show that Ncorr produces a more homogeneous strain distribution whereas DaVis FFT calculates more intense deformation in the slip traces.

The differences in strain localisation were quantified further, using line profiles perpendicular to the slip traces, in terms of both strain and the raw displacements, Figure 9. The position of the line profile is shown by the white dashed line on the effective in-plane shear strain maps for the single grain in Figure 9a. The line profiles of both the effective in-plane shear strain (Figure 9b) and strain in the loading direction (Figure 9c) for each strain step are all similar for DaVis FFT, DaVis LSM and Ncorr with only a slight difference in the intensity of the peaks. In contrast, VIC-2D calculates significantly higher strain in many traces and negative strain in the loading direction in others. Figure 9d shows that the u displacement values from Ncorr at 1% applied strain are similar to those from VIC-2D rather than DaVis FFT and DaVis LSM, whilst the v displacements for Ncorr, Figure 9e, are opposite in direction to those from VIC-2D, DaVis FFT and DaVis LSM. The displacements from Ncorr and VIC-2D also suggest that the strain is changing in between the individual slip traces with positive displacement slopes between slip bands for the Y displacement component for VIC2D compared to negative values for NCorr. In comparison, DaVis FFT and DaVis LSM indicate the majority of the deformation is accommodated in the slip bands and the strain is very small between them, which is the expected response of the material based on previous electron channelling contrast imaging (ECCI) work [39] where at lower strains thin, widely spaced slip bands were observed with little contrast in between, suggesting little deformation in these regions, in high-Mn lightweight steel exhibiting planar dislocation slip. At higher applied strain, there is a good agreement for all algorithms in terms of both u and v.

Determination of the active slip system

High resolution strain mapping greatly reduces the ambiguity associated with traditional EBSD-based slip analysis by combining it with RDR analysis, which provides a unique solution in terms of the Burger's vector direction of the active slip system. Firstly, the active slip modes for a single grain were predicted using the EBSD-based slip trace analysis technique, where the slip traces obtained by HRDIC were compared with all theoretical slip trace angles calculated from the orientation data, Figure 10. The experimental angle was determined by averaging 4 slip traces, highlighted by red dots in Figure 10a, that appear to be parallel. The theoretical slip trace angle projections were then calculated for all the 24 slip systems under consideration (basal $\vec{a}$ (3), prismatic $\vec{a}$ (3), pyramidal $\vec{a}$ (6) and pyramidal 1st order $\vec{c}+\vec{a}$ (12)) and compared to the experimentally measured value using an acceptance criterion of ±5°, shown in Figure 10b by the dashed lines and shadows. The configuration of slip traces in the grain is relatively simple, with the slip traces typically planar and aligned at an angle of ~120° from the loading direction. According to the traditional EBSD-based slip trace analysis, the active slip system is predicted to be prismatic $\vec{a}$ slip, with a Schmid factor of approximately 0.44 for a single $\vec{a}$ direction.

As the traditional slip trace analysis provided a unique solution in terms of the active slip system, RDR analysis was performed for each algorithm to determine the uncertainty of the displacement data. The displacement gradient for each of the 4 slip traces was calculated by firstly drawing a straight line down the centre of each slip trace and then identifying a series of data points that coincide with this line. For each of these data points, a point perpendicular to the slip trace centre line was chosen on either side of the slip trace. The u and v displacement values for each set of 3 points were then centred by subtracting the average u and v values along each line of 3 points. The centred u versus v values were then plotted for each of the algorithms at both strain steps, Figure 11, and the averaged RDR for all 4 slip traces is calculated as the gradient of the linear regression. The theoretical RDR for each of the 24 slip systems was calculated as the ratio between the x-component and y-component of the Burgers vector. R^2, which is a statistical measure of how close the data are to the fitted regression line, was used to evaluate the confidence in the u and v displacement data for calculating the RDR value.

DaVis FFT, DaVis LSM and Ncorr all had R^2 values greater than 0.90 for both strain steps whilst VIC-2D had R^2 values of only 0.35 and 0.57 at 1% and 5% applied strain, respectively. The 3 algorithms with a high R^2value all identified an $\vec{a}$ direction Burgers vector with an RDR value of 0.74, 0.76 and 0.69 (DaVis FFT, DaVis LSM and Ncorr) compared to a theoretical value of 0.75 that corresponded to the slip system predicted by the traditional slip trace analysis. However, VIC-2D identified a different $\vec{a}$ Burgers vector with an RDR value of -0.47. At the higher strain step, the difference between the theoretical and experimental RDR values was larger, which is attributed to an increased contribution from lattice rotation with higher applied strain. The data from VIC-2D at the higher applied strain step appears to suggest the correct $\vec{a}$ Burgers vector. Although, there is significant noise compared to the other algorithms. This indicates that even if the slip traces can be observed from the strain map, the accuracy of the u and v displacements around the slip trace is not guaranteed and care must be taken when performing more detailed analysis as it may lead to an inaccurate prediction of the Burgers vector.

Slip trace identification

Displacement and strain measurements calculated using DIC are highly dependent on the analysis parameters, such as interrogation window size and step size. For example, high strain concentrations like slip bands are unlikely to be fully captured if a large interrogation window size is used as this

averages out the high strain intensities. The minimum size of the interrogation window is controlled by the quality of the pattern and is chosen to provide the optimal balance between spatial resolution and data reliability [29]. Therefore, in the majority of current HRDIC studies, the large displacement gradients across slip traces are not observed and appear as more continuous displacement gradients. However, Figure 12a shows clear steps in the u displacement when intersecting each slip trace for a line profile plotted perpendicular to a set of slip bands in a single grain. From the Ncorr data the steps in displacement are still observed although the profiles do show a slight gradient in the strain between the traces, which suggests the DaVis FFT algorithm is more reliable. The high spatial resolution of the measurements is further emphasised with at least one or two data points calculated in between the displacement steps for each slip trace suggesting slip band widths of 200-400 nm. Moreover, the strain profile, Figure 12b, clearly shows the high strain peaks at the slip trace interface. Recently, the Heaviside DIC method [23] has been developed to detect sharp discontinuities such as slip bands enabling further analysis in terms of slip system identification and the magnitude of strain at the discontinuity. Figure 12 shows similar results to those observed from Heaviside DIC with a clear step across the slip band and high strain values detected in the slip trace region. However, there is a distinct difference in the displacement profiles, where results for the Heaviside based method show negative displacement tails approaching the slip trace, which is probably an artefact of the method. The results shown here indicate that provided the spatial resolution of the HRDIC measurement is high enough, the sharpness of slip bands can be quantified using conventional DIC algorithms. This is important since the thickness of the slip band might be of interest. For example, Thomas et al. resolved strain localisation in an irradiated Zirconium alloy at a spatial resolution of 78 by 78 nm^2, and was able to measure shear strain at several points across a slip band [31].

Implications

The results here show that when deformation is relatively homogeneous the importance of the algorithm used to perform the DIC analysis is less significant, as the displacement of individual features in the deformed condition relative to the undeformed condition will be small and also the surface degradation in relation to the amount of deformation will be limited. This means that the features will be comparatively easy to track using each algorithm. In contrast, when the slip is intense the local displacement across a slip trace boundary will be greater and may lead to separation between speckles in that region leading to the requirement for a suitable feature detection procedure to enable a good correlation. In the heterogeneous case VIC-2D had difficulty correlating the features, particularly in the case of high strain features such as individual slip traces or at grain/phase boundaries. Figure 13 compares the results using the initial analysis parameters for VIC-2D and DaVis LSM, given in Table 1, with different analysis parameters for VIC-2D to see if improvements can be made to the correlation for this software package. Figure 13a shows the initial strain map generated from the original displacement data and it can be observed that by increasing the interrogation window size to provide more features to track, Figure 13b, many of the regions still remain uncorrelated and the overall spatial resolution is reduced. However, by applying a refined step size of 3 x 3 $pixels^2$ (Figure 13c), a significant improvement is found with a strain map that looks more similar to the one produced by DaVis LSM, Figure 13d, with only a few remaining artefacts at slip traces that also have a correlation value of ~0.6 when using the DaVis algorithms. Importantly, it can be concluded that each algorithm requires optimisation of the analysis parameters to produce a good correlation. In this study similar analysis parameters were used for the main comparison to enable a detailed study of the resulting displacement and strain maps.

Ncorr was generally in agreement with both of the DaVis algorithms for both materials thereby making it a reliable open source alternative for HRDIC analysis. The main downside to using the open source alternative is the increased processing time for the displacement calculation. For a 4 x 4 matrix of images Ncorr was found to be ~10-20 times slower than the other algorithms when running using Matlab. This is a particular concern given the recent advancement in automated stage mapping for image capture in a SEM combined with the application of well distributed high-resolution speckle patterns, which has opened up the possibility to measure sub-grain scale deformation over a representative number of grains. Recent high-resolution deformation mapping across a large region [31] captured 256 images covering an area of ~ 200 × 180 μm^2 at a spatial resolution of 0.08 µm. This took around 14 minutes using DaVis FFT, with the settings used for Zircaloy-4 in this work. Using the GPU acceleration or distributed computing features present in DaVis 8.4.0, it may be possible to reduce this further. It should be noted that the graphical user interface slowed down significantly when viewing the 500MB input images. Above this size neither the images nor the output can be viewed without difficulty in DaVis, however they can be visualised using the in-house Python package. The current size limit for input images in DaVis 8.4.0 is around 1.5GB. It is not known whether the open-source software has the capability of handling such a large dataset and the time taken to perform the calculation is likely to be considerably longer. However, the Ncorr code does allow for multi-threading, which should speed up the DIC analysis, when utilizing multicore processors.

In summary, from the results for the different software packages and algorithms it is possible to determine the algorithm that has the most potential in terms of sharp discontinuity analysis. Firstly, DaVis LSM and FFT exhibited the expected behaviour in regard to the displacement profiles across individual slip traces at low strains with little deformation between the traces and large displacement jumps at the discontinuity, as previously observed by Bourdin et al [23]. Conversely, NCorr and VIC-2D showed opposite positive and negative displacement slopes between slip bands for the X and Y displacements. For NCorr, this did not appear to have a significant impact on the subsequent RDR analysis as the same Burgers vector was predicted as DaVis LSM and FFT with only a slight reduction in the confidence value. VIC-2D also had difficulty in the tracking of the interrogation windows at these sharp discontinuities, that could be improved by modifying the analysis parameters but still had issues at particular slip traces.

Conclusions

HRDIC analysis was conducted using established commercial (DaVis and VIC-2D) and open-source (Ncorr) software packages with equivalent parameters to evaluate whether the software used to calculate the displacements can have an impact on the full-field displacement and strain maps. Two different materials were investigated, Zircaloy-4 exhibiting relatively diffuse and homogeneous slip and Ti-6Al-4V with sharp, planar slip traces. Little difference was observed in the displacement and strain values for Zircaloy-4 however VIC-2D had issues tracking the features in the case of Ti-6Al-4V particularly at the low strain step where the strain concentrations can be up to 20 times higher than the strain in the loading direction. This not only led to visually aberrant strain maps but also an incorrect prediction of the Burgers vector of the active slip system using the Relative Displacement Ratio technique. Furthermore, it was shown that the high spatial resolution of the measurements enabled the displacement fields around slip bands to be quantified with clear steps in the displacement from one side of a slip band to another observed.

Data availability

The raw/processed data required to reproduce these findings cannot be shared at this time due to technical or time limitations.

Declaration of Competing interest

The authors declare that they have no known competing financial interests or personal relationships that could have appeared to influence the work reported in this paper.

Acknowledgement

The authors would like to thank the Engineering and Physical Sciences Research Council UK (EPSRC) for funding the study through EP/K034332/1 and EP/I005420/1. The authors would also like to thank Rolls-Royce for providing material and financial contribution to Rhys Thomas's PhD studentship.

Reference

[1] F. Hild and S. Roux, "Digital image correlation: from displacement measurement to identification of elastic properties - a Review," *Strain*, vol. 42, no. 2, pp. 69–80, 2006.

[2] F. Hild and S. Roux, "Comparison of Local and Global Approaches to Digital Image Correlation," *Exp. Mech.*, pp. 1503–1519, Mar. 2012.

[3] M. a. Sutton and F. Hild, "Recent Advances and Perspectives in Digital Image Correlation," *Exp. Mech.*, no. February, pp. 1–8, 2015.

[4] B. Pan, K. Li, and W. Tong, "Fast, Robust and Accurate Digital Image Correlation Calculation Without Redundant Computations," *Exp. Mech.*, vol. 53, no. 7, pp. 1277–1289, 2013.

[5] J. Quinta Da Fonseca, P. M. Mummery, and P. J. Withers, "Full-field strain mapping by optical correlation of micrographs," *J. Microsc.*, vol. 218, no. April, pp. 9–21, 2005.

[6] D. Lunt, J. Quinta da Fonseca, D. Rugg, and M. Preuss, "Microscopic strain localisation in Ti-6Al-4V during uniaxial tensile loading," *Mater. Sci. Eng. A*, vol. 680, no. 680, pp. 444–453, 2017.

[7] P. D. Littlewood and A. J. Wilkinson, "Local deformation patterns in Ti–6Al–4V under tensile, fatigue and dwell fatigue loading," *Int. J. Fatigue*, vol. 43, pp. 111–119, Oct. 2012.

[8] W. Z. Abuzaid, M. D. Sangid, J. D. Carroll, H. Sehitoglu, and J. Lambros, "Slip transfer and plastic strain accumulation across grain boundaries in Hastelloy X," *J. Mech. Phys. Solids*, 2012.

[9] M. Sachtleber, Z. Zhao, and D. Raabe, "Experimental investigation of plastic grain interaction," *Mater. Sci. Eng. A*, 2002.

[10] J. Carroll, W. Abuzaid, J. Lambros, and H. Sehitoglu, "An experimental methodology to relate local strain to microstructural texture," *Rev. Sci. Instrum.*, vol. 81, no. 8, 2010.

[11] M. Bertin, C. Du, J. P. M. Hoefnagels, and F. Hild, "Crystal plasticity parameter identification with 3D measurements and Integrated Digital Image Correlation," *Acta Mater.*, 2016.

[12] J. H. Liu, N. Vanderesse, J. C. Stinville, T. M. Pollock, P. Bocher, and D. Texier, "In-plane and out-of-plane deformation at the sub-grain scale in polycrystalline materials assessed by confocal microscopy," *Acta Mater.*, 2019.

[13] A. Orozco-Caballero, D. Lunt, J. D. J. D. Robson, and J. Quinta da Fonseca, "How magnesium

accommodates local deformation incompatibility : A high-resolution digital image correlation study," *Acta Mater.*, vol. 133, pp. 367–379, 2017.

[14] T. E. J. Edwards, F. Di Gioacchino, H. P. Springbett, R. A. Oliver, and W. J. Clegg, "Stable speckle patterns for nano-scale strain mapping up to 700 ° C Stable Speckle Patterns for Nano-scale Strain Mapping up to 700 ° C," *Exp. Mech.*, no. July, 2017.

[15] P. Platt, D. Lunt, E. Polatidis, M. R. Wenman, and M. Preuss, "In-situ Digital Image Correlation for Fracture Analysis of Oxides Formed on Zirconium Alloys," *Corros. Sci.*, vol. 111, 2016.

[16] Y. B. Das *et al.*, "In situ observation of strain and phase transformation in plastically deformed 301 austenitic stainless steel," *Mater. Des.*, vol. 112, pp. 107–116, 2016.

[17] Z. Chen, W. Lenthe, J. C. Stinville, M. Echlin, T. M. Pollock, and S. Daly, "High-Resolution Deformation Mapping Across Large Fields of View Using Scanning Electron Microscopy and Digital Image Correlation," *Exp. Mech.*, p. Accepted, 2018.

[18] J. C. Stinville, M. P. Echlin, D. Texier, F. Bridier, P. Bocher, and T. M. Pollock, "Sub-Grain Scale Digital Image Correlation by Electron Microscopy for Polycrystalline Materials during Elastic and Plastic Deformation," *Exp. Mech.*, vol. 56, no. 2, pp. 197–216, 2016.

[19] A. D. Kammers and S. Daly, "Digital Image Correlation under Scanning Electron Microscopy: Methodology and Validation," *Exp. Mech.*, vol. 53, no. 9, pp. 1743–1761, 2013.

[20] J. Jiang, T. Ben Britton, and A. J. Wilkinson, "The orientation and strain dependence of dislocation structure evolution in monotonically deformed polycrystalline copper," *Int. J. Plast.*, vol. 69, pp. 102–117, Jun. 2015.

[21] Z. Chen and S. H. Daly, "Active Slip System Identification in Polycrystalline Metals by Digital Image Correlation (DIC)," *Exp. Mech.*, no. Dic, 2016.

[22] J. C. Stinville, W. C. Lenthe, M. P. Echlin, P. G. Callahan, D. Texier, and T. M. Pollock, "Microstructural statistics for fatigue crack initiation in polycrystalline nickel-base superalloys," *Int. J. Fract.*, vol. 208, no. 1–2, pp. 221–240, 2017.

[23] F. Bourdin *et al.*, "Measurements of plastic localization by heaviside-digital image correlation," *Acta Mater.*, vol. 157, pp. 307–325, 2018.

[24] T. A. Book and M. D. Sangid, "Materials Characterization Strain localization in Ti-6Al-4V Widmanstätten microstructures produced by additive manufacturing," *Mater. Charact.*, vol. 122, pp. 104–112, 2016.

[25] W. N. Hsu, E. Polatidis, M. Šmíd, N. Casati, S. Van Petegem, and H. Van Swygenhoven, "Load path change on superelastic NiTi alloys: In situ synchrotron XRD and SEM DIC," *Acta Mater.*, vol. 144, pp. 874–883, 2018.

[26] V. Belloni, R. Ravanelli, A. Nascetti, M. Di Rita, D. Mattei, and M. Crespi, "Digital image correlation from commercial to FOS software: A mature technique for full-field displacement measurements," *Int. Arch. Photogramm. Remote Sens. Spat. Inf. Sci. - ISPRS Arch.*, vol. 42, no. 2, pp. 91–95, 2018.

[27] R. Harilal and M. Ramji, "Adaptation of Open Source 2D DIC Software Ncorr for Solid Mechanics Applications," *9th Int. Symp. Adv. Sci. Technol. Exp. Mech.*, no. November, pp. 1–6, 2014.

[28] E. Dall'Asta, V. Ghizzardi, R. Brighenti, E. Romeo, R. Roncella, and A. Spagnoli, "New experimental techniques for fracture testing of highly deformable materials," *Frat. ed Integrita Strutt.*, vol. 10, no. 35, pp. 161–171, 2016.

[29] D. Lunt, T. Busolo, X. Xu, J. Q. Fonseca, and M. Preuss, “Effect of nanoscale α2 precipitation on strain localisation in a two--phase Ti-alloy,” *Acta Mater.*, 2017.

[30] D. Lunt, T. Busolo, X. Xu, J. Quinta da Fonseca, and M. Preuss, “Effect of nanoscale α2 precipitation on strain localisation in a two-phase Ti-alloy,” *Acta Mater.*, 2017.

[31] R. Thomas *et al.*, “Characterisation of irradiation enhanced strain localisation in Zr alloys,” *Materialia*, 2019.

[32] F. Di Gioacchino and J. Quinta Da Fonseca, “An experimental study of the polycrystalline plasticity of austenitic stainless steel,” *Int. J. Plast.*, vol. 74, pp. 92–109, 2015.

[33] D. Lunt *et al.*, “Enabling high resolution strain mapping in zirconium alloys,” *Mater. Charact.*, vol. 139, no. December 2017, pp. 355–363, 2018.

[34] J. Schindelin *et al.*, “Fiji: An open-source platform for biological-image analysis,” *Nat. Methods*, vol. 9, no. 7, pp. 676–682, 2012.

[35] LaVision, “DaVis.” La Vision, Germany.

[36] S. Van Der Walt, S. C. Colbert, and G. Varoquaux, “The NumPy array: A structure for efficient numerical computation,” *Comput. Sci. Eng.*, vol. 13, no. 2, pp. 22–30, 2011.

[37] J. D. Hunter, “Matplotlib: A 2D Graphics Environment,” *Comput. Sci. Eng.*, pp. 90–95, 2007.

[38] F. Bridier, P. Villechaise, and J. Mendez, “Analysis of the different slip systems activated by tension in a alpha+beta titanium alloy in relation with local crystallographic orientation,” *Acta Materialia*, vol. 53, no. 3. pp. 555–567, Feb-2005.

[39] E. Welsch *et al.*, “Strain hardening by dynamic slip band refinement in a high-Mn lightweight steel,” *Acta Mater.*, vol. 116, pp. 188–199, 2016.

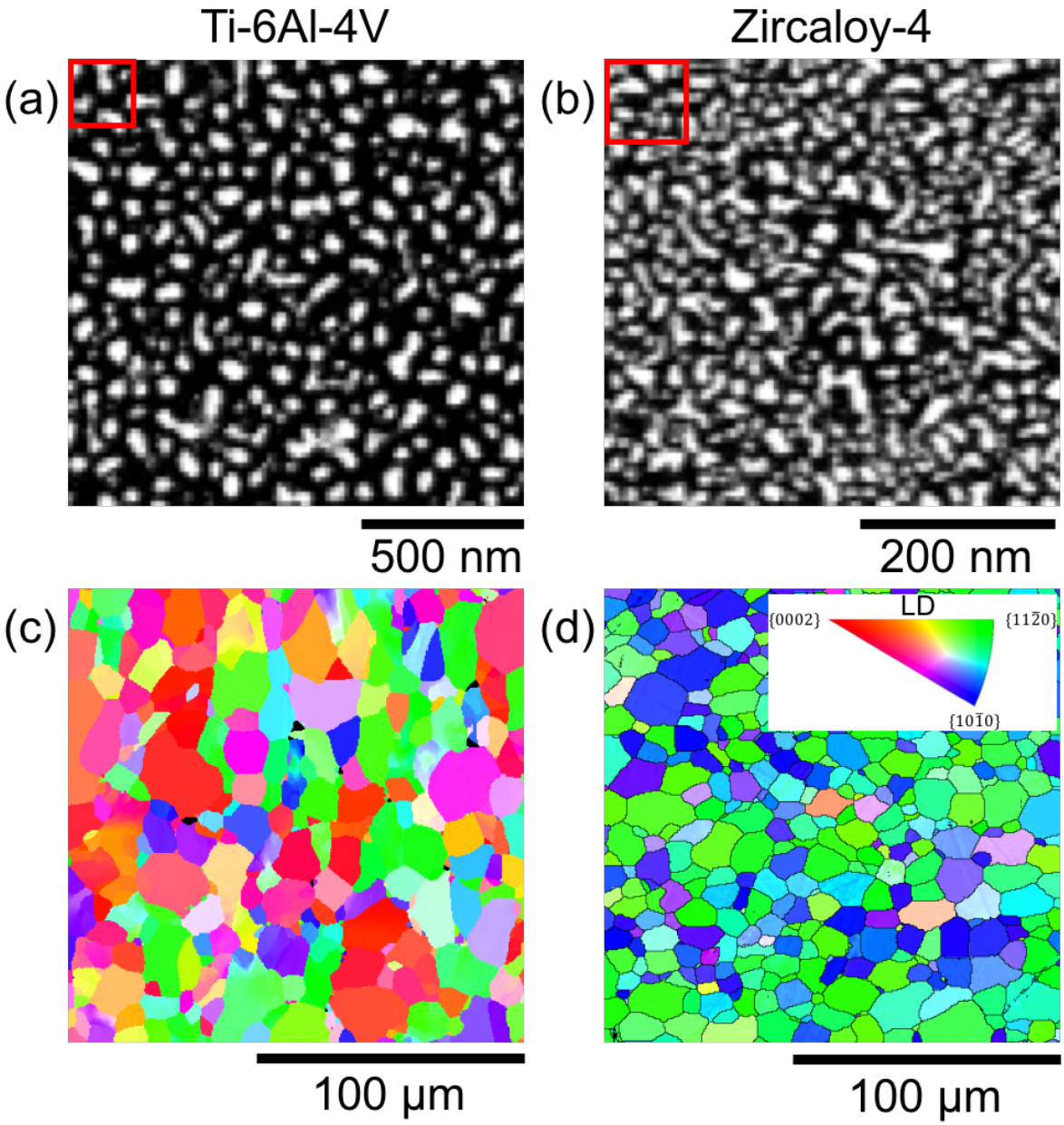

Figure 1- Speckle pattern at pixel scale resolution for (a) Ti-6Al-4V and (b) Zircaloy-4, with interrogation window size indicated in red, and representative IPF LD map for (c) Ti-6Al-4V and (d) Zircaloy-4.

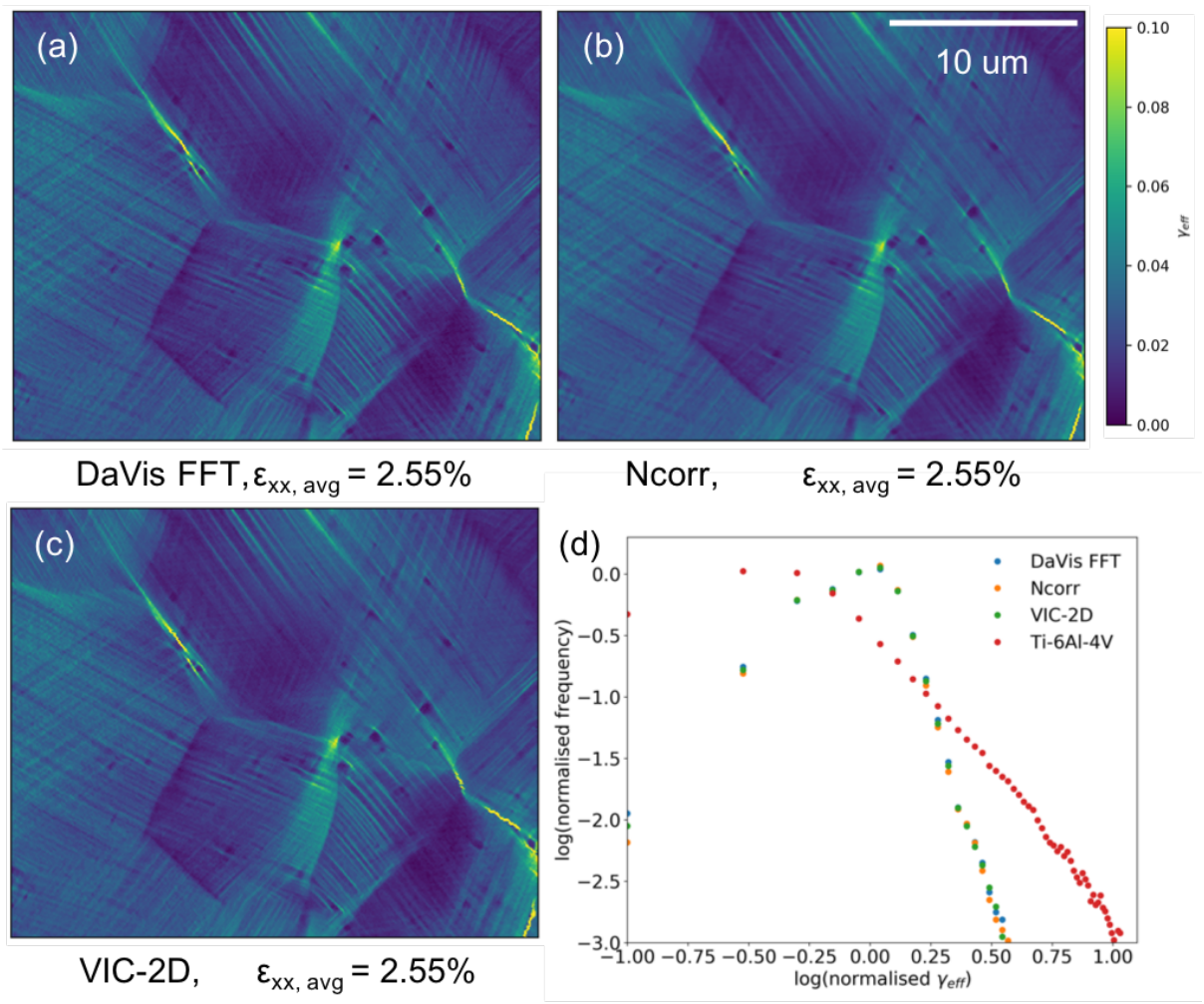

Figure 2- Effective in-plane shear strain maps at ~2.5% for Zircaloy-4 loaded along RD generated using displacement data from (a) DaVis FFT, (b) Ncorr and (c) VIC-2D and (d) the normalised frequency distribution of the normalised effective in-plane shear strain for the different algorithms along with a comparison to Ti-6Al-4V data (DaVis FFT) at 1% applied strain

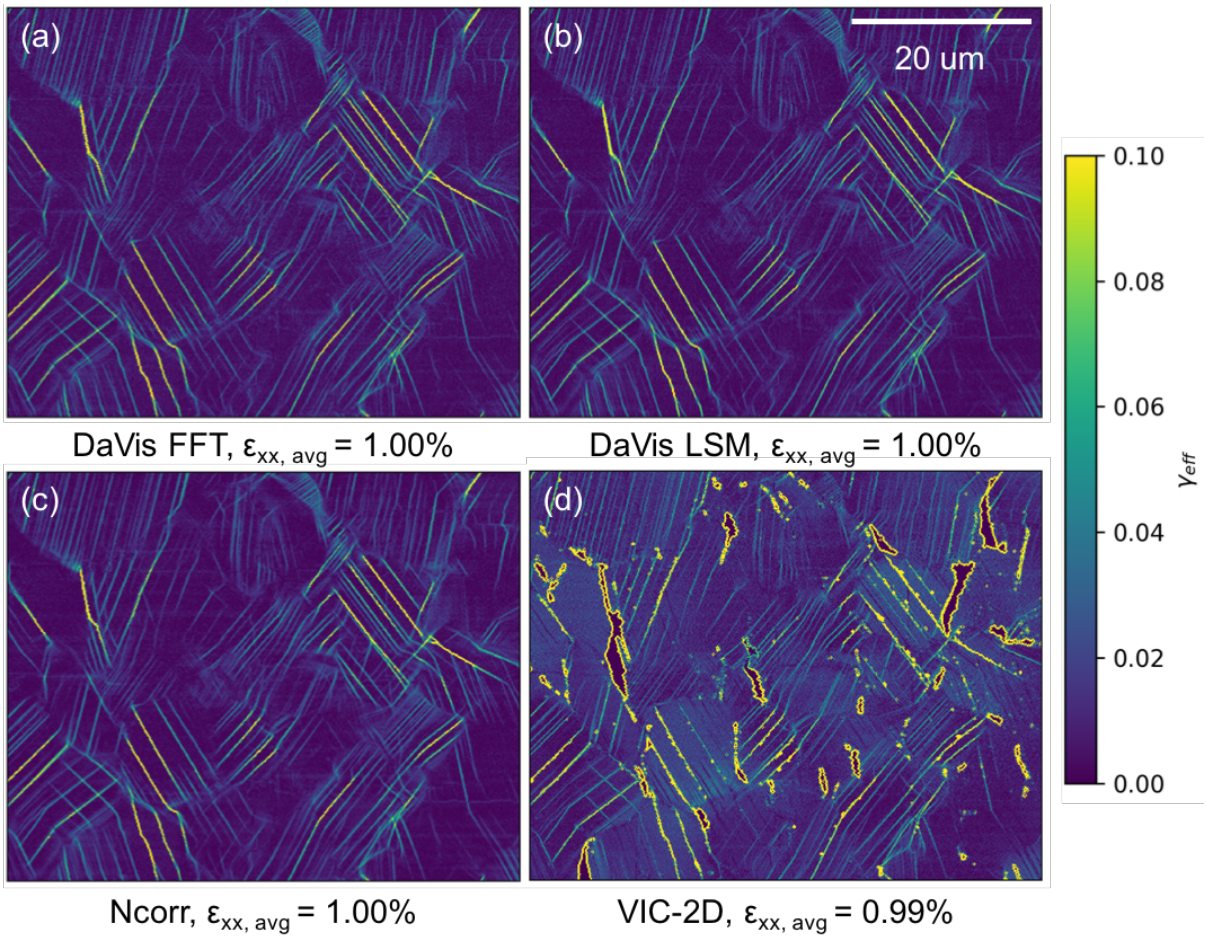

Figure 3- Effective in-plane shear strain maps for Ti-6Al-4V at ~1.0% applied strain, generated using displacement data from (a) DaVis FFT, (b) DaVis LSM, (c) Ncorr and (d) VIC-2D

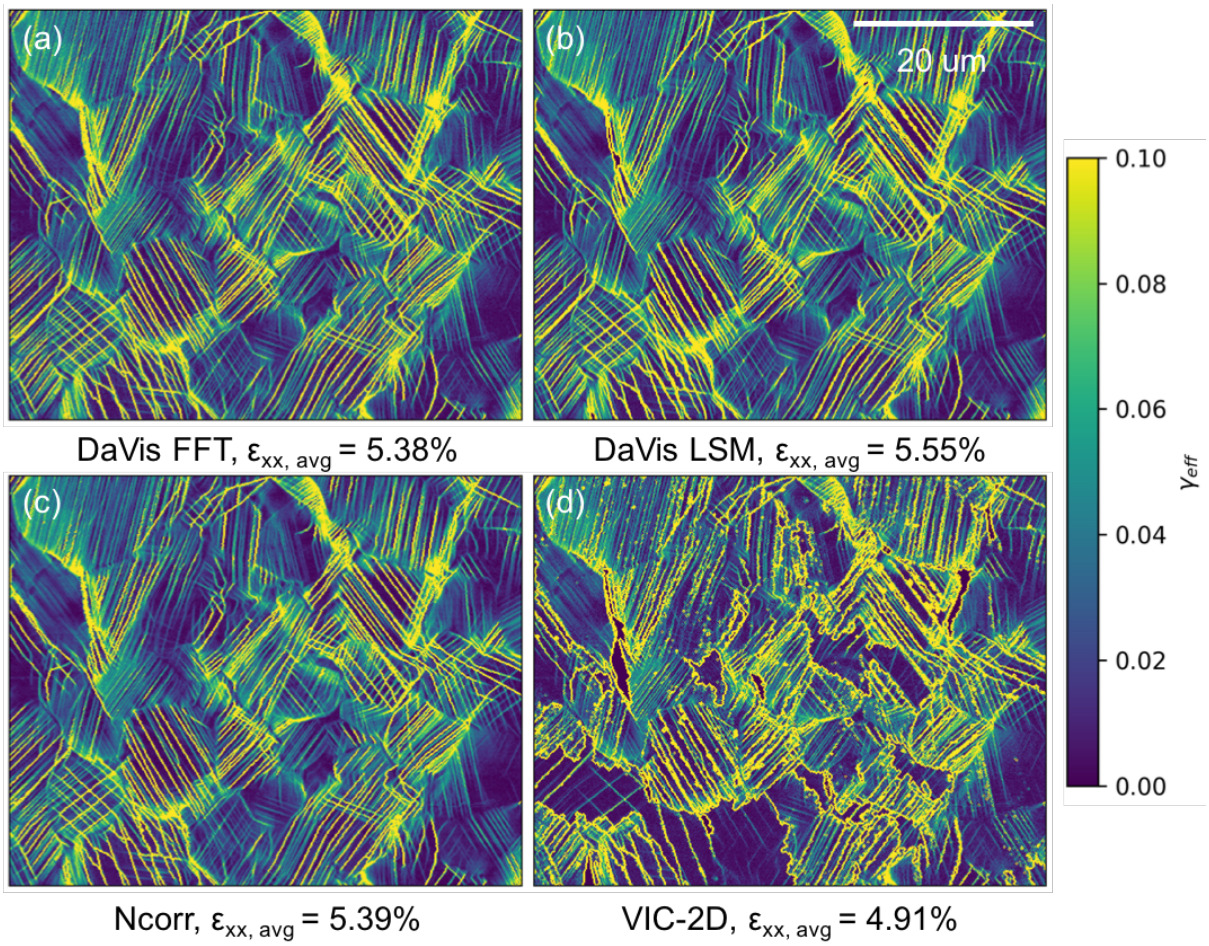

Figure 4- Effective in-plane shear strain maps for Ti-6Al-4V at ~5.0% applied strain, generated using displacement data from (a) DaVis FFT, (b) DaVis LSM, (c) Ncorr and (d) VIC-2D

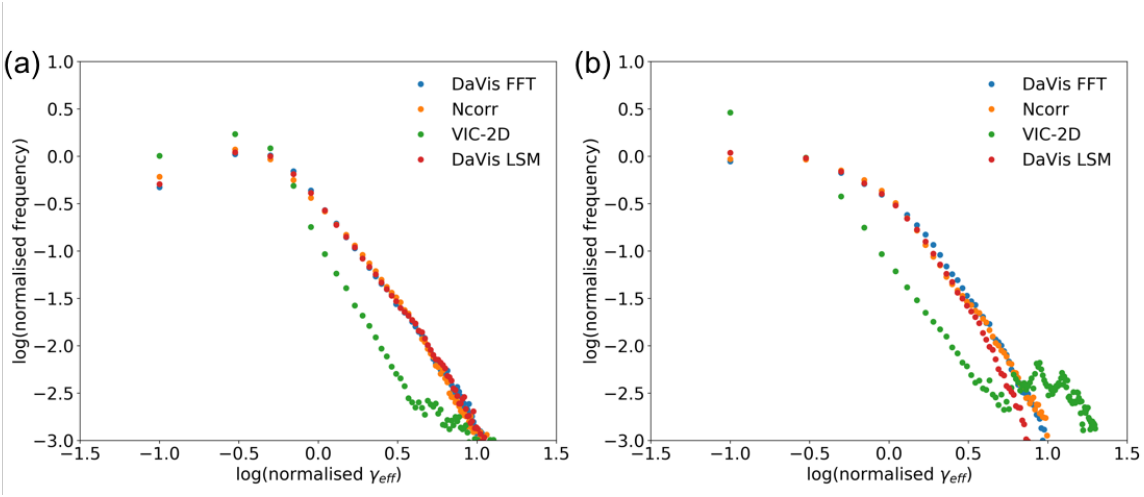

Figure 5- Normalised frequency distribution of normalised effective in-plane shear strain for the different algorithms at (a) ~1% and (b) ~5% applied strain for Ti-6Al-4V for the complete HRDIC region

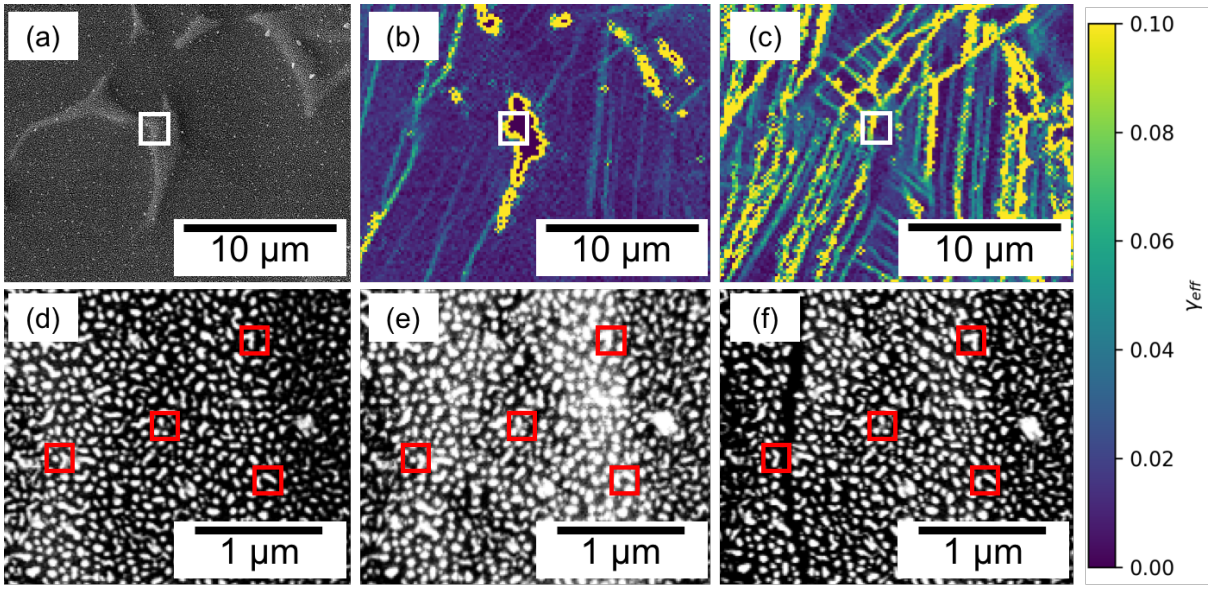

Figure 6- (a) BSE image from before deformation with corresponding maps of effective shear at (b) ~1% and (c) ~5% applied strain. Speckle patterns, at pixel scale resolution, from (d) before deformation, (e) ~1% and (f) ~5% applied strain from the areas highlighted with a white box in (a)-(c). The red boxes indicate the distinct features that are easily tracked visually from each deformation stage.

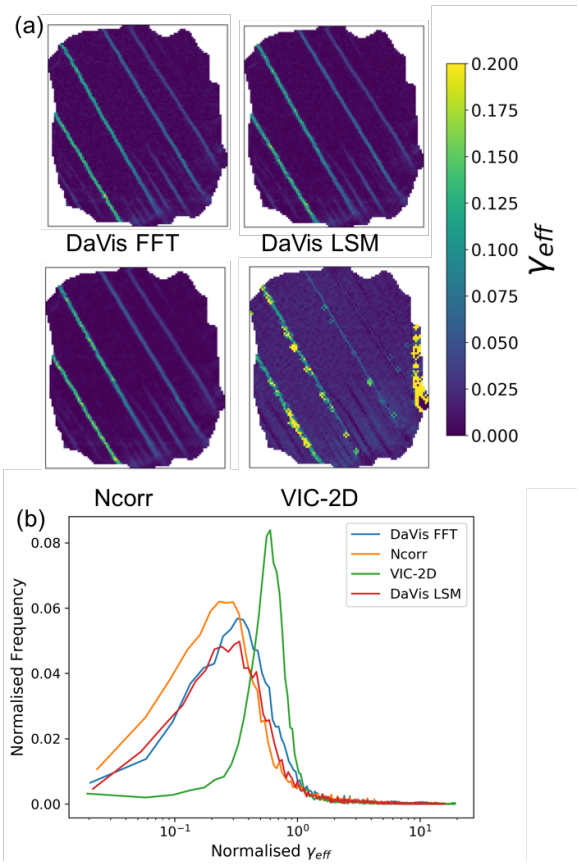

Figure 7- Effective in-plane shear strain maps for Ti-6Al-4V in a single grain at ~1% applied strain, generated using displacement data from DaVis FFT, DaVis LSM, Ncorr and VIC-2D, respectively, and (b) normalised frequency distribution of normalised effective in-plane shear strain for each algorithm.

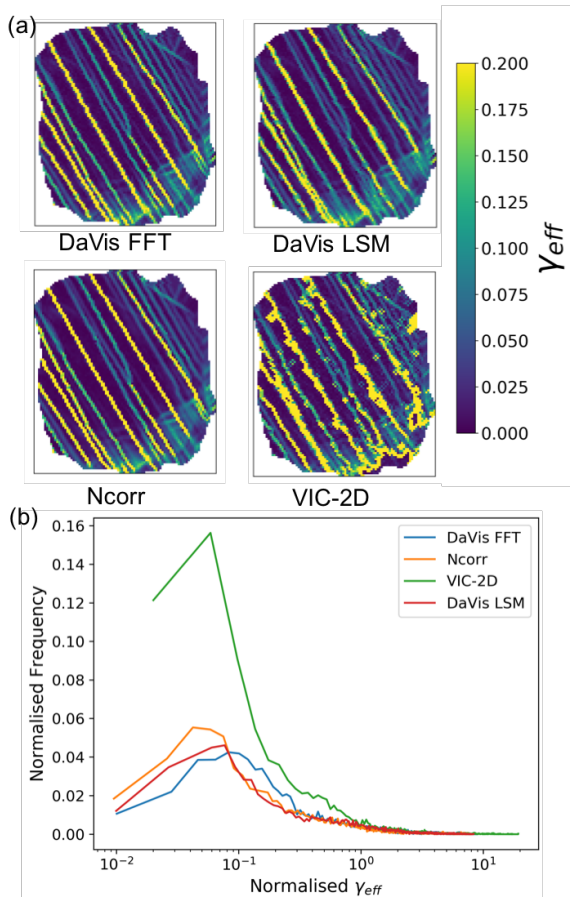

Figure 8- Effective in-plane shear strain maps for Ti-6Al-4V in a single grain at ~5% applied strain, generated using displacement data from DaVis FFT, DaVis LSM, Ncorr and VIC-2D, respectively, and (b) normalised frequency distribution of normalised effective in-plane shear strain for each algorithm.

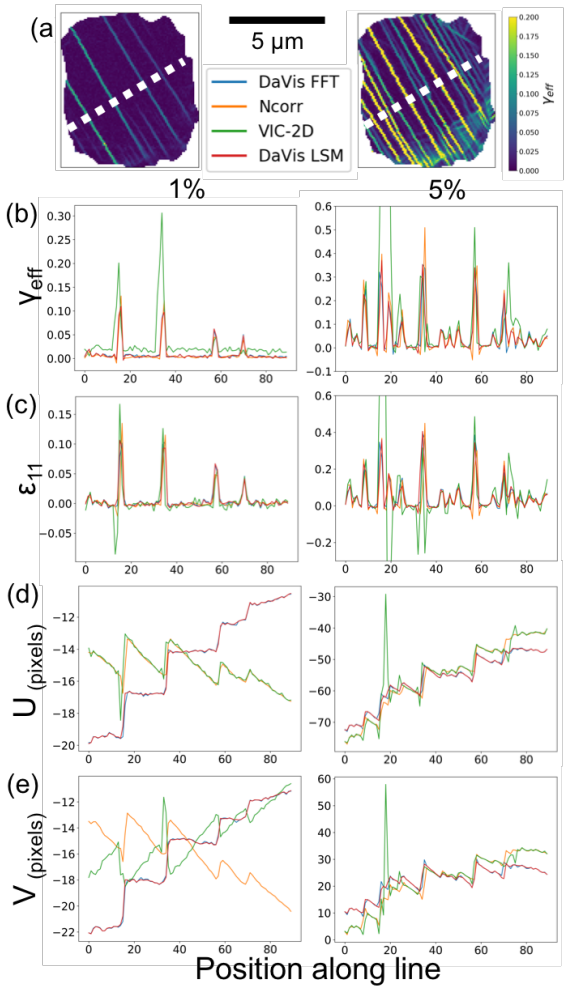

Figure 9- Profile plots, along the white dashed line shown in (a) the maps of effective in-plane shear strain for a single grain, of (b) effective in-plane shear strain, (c) strain in the loading direction, (d) x displacement and (e) y displacement at ~1% and 5% applied strain, respectively, for each algorithm.

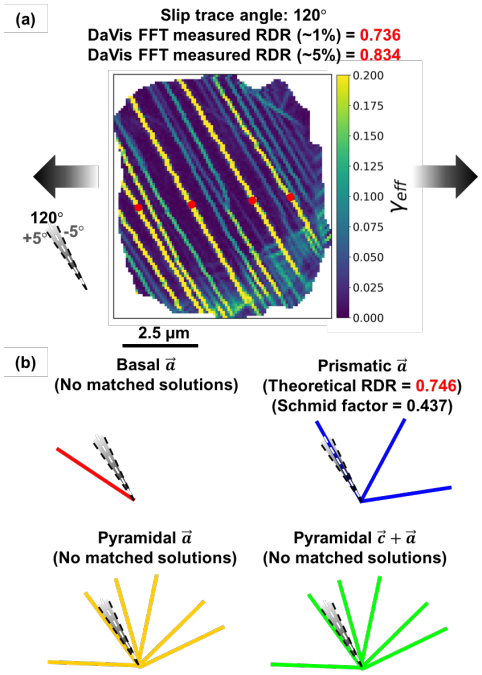

Figure 10- (a) effective in-plane shear strain map and (b) projections for all possible slip systems compared with the experimental slip traces marked with red dots. The dashed lines/shadows on the schematics show the ±5° range from the experimentally measured slip trace angle.

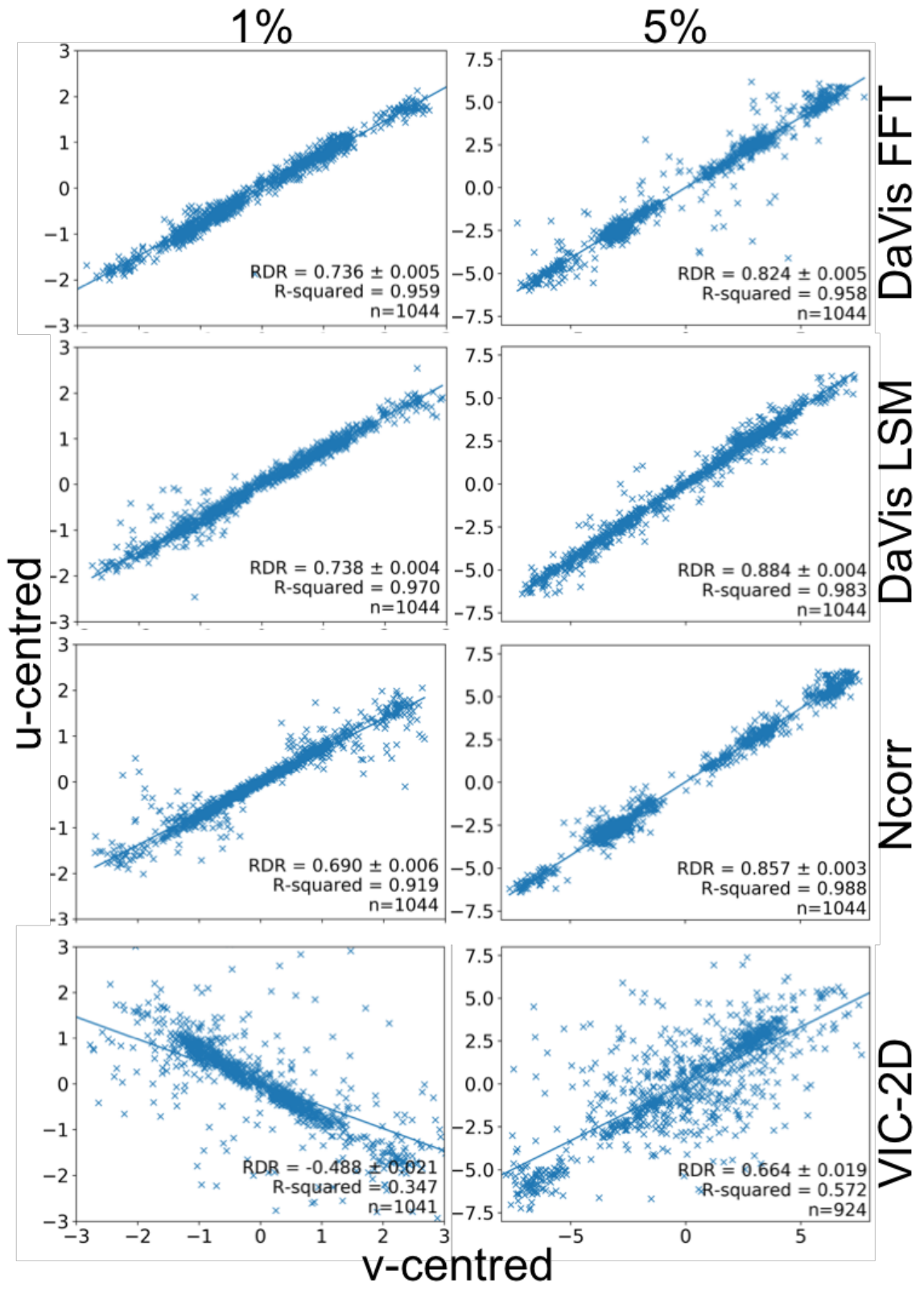

Figure 11- Centered u and v values taken from the neighbourhood of 4 slip traces for grain 1 for DaVis FFT, DaVis LSM, Ncorr and VIC-2D at ~1% and 5% applied strain, respectively. The RDR value is the gradient of the line, R-squared is the coefficient of determination and n is the number of points.

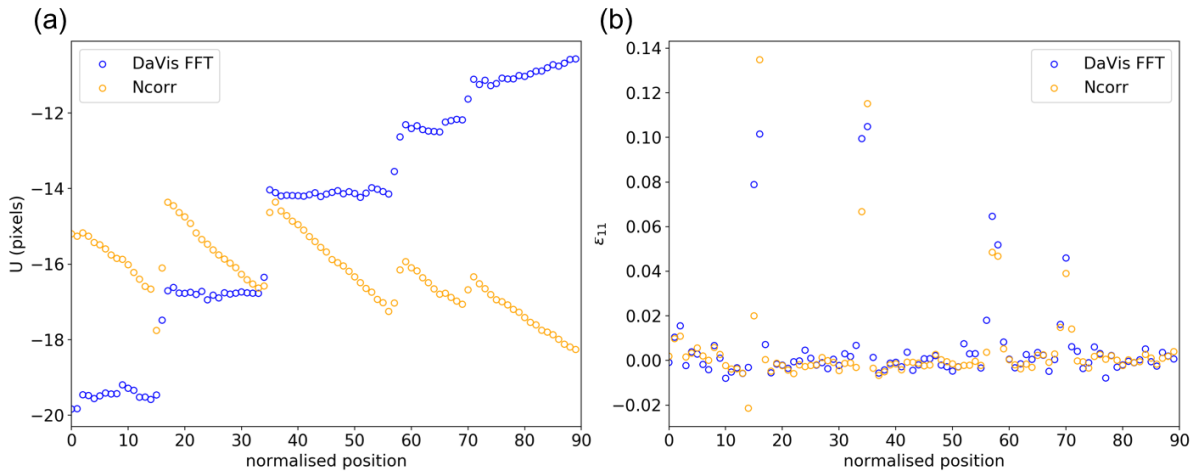

Figure 12- Scatter plots, along the white dashed line shown in Figure 9a, of (a) x displacement and (b) strain in the loading direction at ~1% applied strain for DaVis FFT and Ncorr

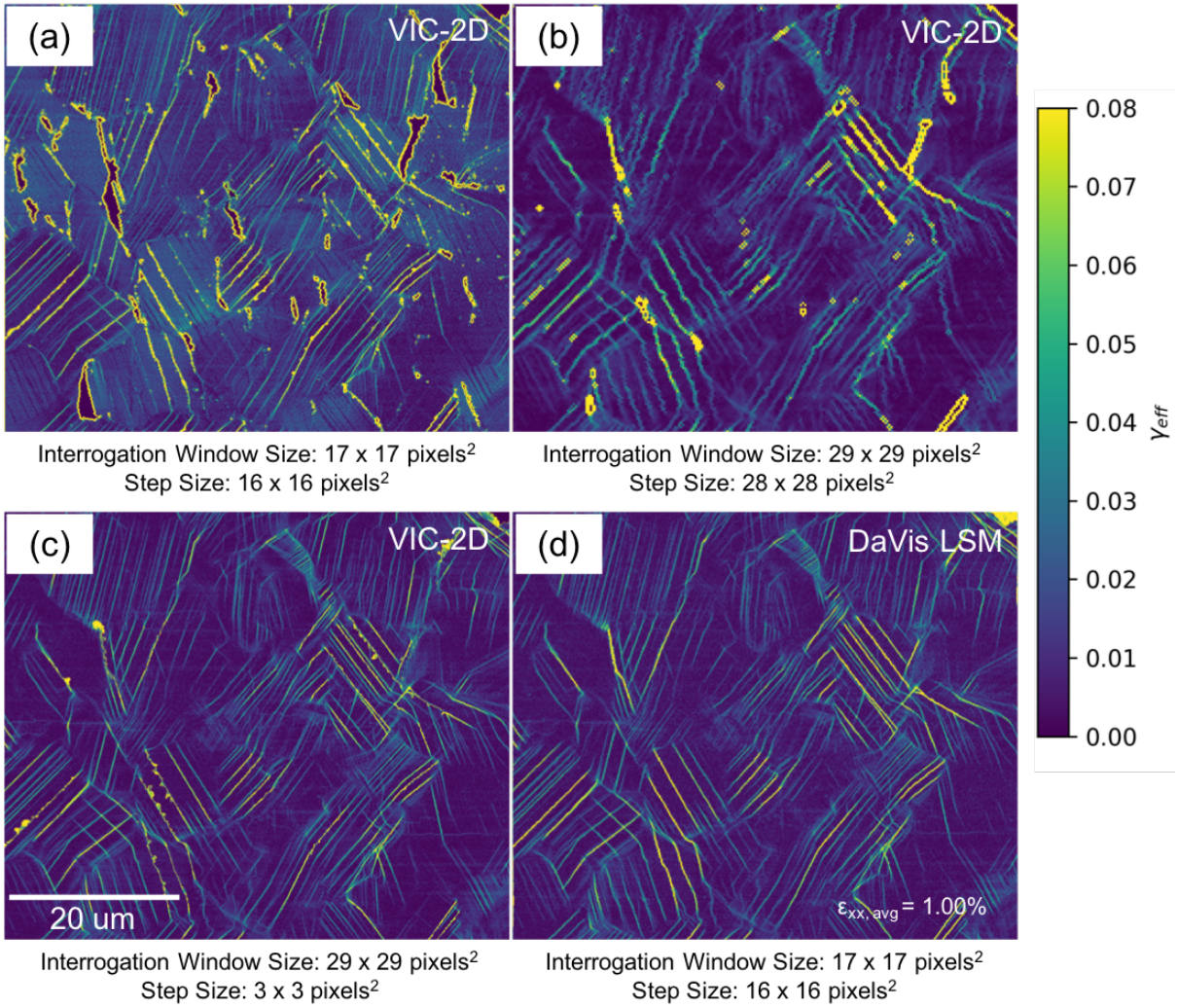

Figure 13- Effective in-plane shear strain maps for Ti-6Al-4V at ~1.0% applied strain, generated using displacement data from (a), (b) and (c) VIC-2D using three different sets of parameters, given in the figure, in comparison to (d) DaVis LSM

Table 1- Comparison of analysis parameters and processing time with single image resolution of 2048 x 1768 pixels^2.

	Zircaloy-4		Ti-6Al-4V (4 x 4 images stitched)		
Spatial resolution (nm)	78.1		174.6		
Number of interrogation windows	374 x 500		498 x 607		
Single Tile Width (μm)	10		29.8		
Algorithm	**Interrogation Window Size (pixels^2)**	**Step size (pixels^2)**	**Interrogation Window Size (pixels^2)**	**Step size (pixels^2)**	**Processing Time (minutes)**
DaVis FFT[#1]	16 x 16	16 x 16	12 x 12	12 x 12	1.5
Ncorr[#2]	16 x 16	15 x 15	12 x 12	11 x 11	25*
VIC-2D	17 x 17	16 x 16	13 x 13	12 x 12	3.5*
DaVis LSM	17 x 17	16 x 16	13 x 13	12 x 12	3.5*

[#1]Circle interrogation windows with 5 iterations at final window size and high accuracy B-spline applied. [#2]Circle interrogation windows. *Includes time to set seeding points.

Table 2- Summary of EBSD-based slip trace analysis and theoretical RDR analysis for each slip system considered for Ti-6Al-4V grain highlighted in Figure 7.

Slip System Type	Slip System	Schmid Factor	Slip Trace Angle (°)	RDR
Basal $\vec{a}$	(0001) $[11\bar{2}0]$	0.294	146.2	29.613
	(0001) $[1\bar{2}10]$	0.112	146.2	-0.477
	(0001) $[\bar{2}110]$	0.182	146.2	0.746
Prismatic $\vec{a}$	$(10\bar{1}0)$ $[1\bar{2}10]$	0.315	61.9	-0.477
	$(01\bar{1}0)$ $[\bar{2}110]$	0.437	118.9	0.746
	$(1\bar{1}00)$ $[11\bar{2}0]$	0.123	8.4	29.613
Pyramidal $\vec{a}$	$(1\bar{1}01)$ $[11\bar{2}0]$	0.033	178	29.613
	$(1\bar{1}0\bar{1})$ $[11\bar{2}0]$	0.248	25.4	29.613
	$(10\bar{1}1)$ $[1\bar{2}10]$	0.223	44.5	-0.477
	$(10\bar{1}\bar{1})$ $[1\bar{2}10]$	0.330	78.3	-0.477
	$(01\bar{1}1)$ $[\bar{2}110]$	0.471	126.0	0.746
	$(01\bar{1}\bar{1})$ $[\bar{2}110]$	0.297	105.6	0.746
Pyramidal $\vec{c}+\vec{a}$	$(10\bar{1}\bar{1})$ $[11\bar{2}3]$	0.218	78.3	0.575
	$(10\bar{1}\bar{1})$ $[\bar{2}11\bar{3}]$	0.042	78.3	0.057
	$(10\bar{1}1)$ $[\bar{1}\bar{1}23]$	0.477	44.5	-2.027
	$(10\bar{1}1)$ $[\bar{2}113]$	0.359	44.5	26.449
	$(1\bar{1}01)$ $[\bar{2}113]$	0.020	178.0	26.449
	$(1\bar{1}01)$ $[\bar{1}2\bar{1}3]$	0.003	178.0	15.353
	$(1\bar{1}0\bar{1})$ $[1\bar{2}13]$	0.120	25.4	-0.573
	$(1\bar{1}0\bar{1})$ $[\bar{2}11\bar{3}]$	0.012	25.4	0.057
	$(01\bar{1}1)$ $[11\bar{2}3]$	0.191	126.0	0.575

	$(01\bar{1}1)$ $[\bar{1}2\bar{1}3]$	0.060	126.0	15.353
	$(01\overline{\bar{1}1})$ $[\overline{1\bar{1}}23]$	0.390	105.6	-2.027
	$(01\overline{\bar{1}1})$ $[1\bar{2}13]$	0.232	105.6	-0.573